TẠP CHÍ KHOA HỌC
TRƯỜNG ĐẠI HỌC QUY NHƠN

Tổng hợp composite $Co_2[Fe(CN)_6]/g\text{-}C_3N_4$ làm chất xúc tác quang hiệu năng cao phân hủy methylene blue

Võ Như Quỳnh[1], Đỗ Hoàng Chỉnh[2], Nguyễn Thị Quỳnh Giao[2], Trần Thị Thanh Tuyền[2], Trần Thị Phương Diễm[2], Phạm Hồ Khánh Đoan[2], Trương Công Đức[1], Lê Thị Thanh Liễu[1], Nguyễn Thị Việt Nga[2,*], Nguyễn Văn Kim[1,*]

[1]Khoa Khoa học Tự nhiên, Trường Đại học Quy Nhơn, Việt Nam
[2]Khoa Sư phạm, Trường Đại học Quy Nhơn, Việt Nam

Ngày nhận bài: 01/08/2025; Ngày sửa bài: 28/08/2025;
Ngày nhận đăng: 06/10/2025; Ngày xuất bản: 28/02/2026

TÓM TẮT

Trong nghiên cứu này, vật liệu composite $Co_2[Fe(CN)_6]/g\text{-}C_3N_4$ được tổng hợp bằng cách chuẩn bị riêng biệt hai thành phần $g\text{-}C_3N_4$ và $Co_2[Fe(CN)_6]$, sau đó kết hợp chúng thông qua quá trình phân tán $Co_2[Fe(CN)_6]$ lên bề mặt $g\text{-}C_3N_4$ ở 90 °C trong 1 giờ. Các vật liệu thu được được đặc trưng bằng các kỹ thuật nhiễu xạ tia X (XRD), phổ hồng ngoại biến đổi Fourier (FT-IR), phổ tán xạ năng lượng tia X (EDS), hiển vi điện tử quét (SEM), phổ phản xạ khuếch tán UV-Vis (UV-Vis DRS) và phổ phát quang (PL). Hiệu suất xúc tác quang của vật liệu composite được đánh giá thông qua quá trình phân hủy methylene blue (MB) trong dung dịch nước dưới chiếu xạ ánh sáng mặt trời. Vật liệu composite $Co_2[Fe(CN)_6]/g\text{-}C_3N_4$ cho thấy hoạt tính xúc tác quang vượt trội so với từng thành phần riêng lẻ là $g\text{-}C_3N_4$ và $Co_2[Fe(CN)_6]$.

Từ khóa: *$Co_2[Fe(CN)_6]$, $Co_2[Fe(CN)_6]/g\text{-}C_3N_4$, photocatalytic activity, methylene blue, sunlight.*

**Tác giả liên hệ chính.*
Email: nguyenvankim@qnu.edu.vn, nguyenthivietnga@qnu.edu.vn

QUY NHON UNIVERSITY
JOURNAL OF SCIENCE

Synthesis of $Co_2[Fe(CN)_6]/g\text{-}C_3N_4$ composite as an improved photocatalyst for degradation of methylene blue

Vo Nhu Quynh[1], Do Hoang Chinh[2], Nguyen Thi Quynh Giao[2], Tran Thi Thanh Tuyen[2], Tran Thi Phuong Diem[2], Pham Ho Khanh Doan[2], Truong Cong Duc[1], Le Thi Thanh Lieu[1], Nguyen Thi Viet Nga[2,*], Nguyen Van Kim[1,*]

[1]*Faculty of Natural Sciences, Quy Nhon University, Vietnam*
[2]*Faculty of Education, Quy Nhon University, Vietnam*

Received: 01/08/2025; Revised: 28/08/2025;
Accepted: 06/10/2025; Published: 28/02/2026

ABSTRACT

In this study, the $Co_2[Fe(CN)_6]/g\text{-}C_3N_4$ composite was synthesized by first preparing $g\text{-}C_3N_4$ and $Co_2[Fe(CN)_6]$ separately, followed by their coupling through the dispersion of $Co_2[Fe(CN)_6]$ onto $g\text{-}C_3N_4$ at 90 °C for 1 hour. The resulting materials were characterized by X-ray diffraction (XRD), Fourier-transform infrared spectroscopy (FT-IR), energy-dispersive X-ray spectroscopy (EDS), scanning electron microscopy (SEM), UV-Vis diffuse reflectance spectroscopy (UV-Vis DRS), and photoluminescence (PL) spectroscopy. The photocatalytic performance of the composite was evaluated via the degradation of methylene blue (MB) in aqueous solution under sunlight irradiation. The $Co_2[Fe(CN)_6]/g\text{-}C_3N_4$ composite exhibited superior photocatalytic activity compared to the individual components, $g\text{-}C_3N_4$ and $Co_2[Fe(CN)_6]$.

Keywords: *$Co_2[Fe(CN)_6]$, $Co_2[Fe(CN)_6]/g\text{-}C_3N_4$, photocatalytic activity, methylene blue, sunlight.*

1. INTRODUCTION

Faced with the growing reality of seriously polluted water sources that threaten both public health and the environment, various technologies have been developed for wastewater treatment. However, conventional methods often fail to completely eliminate toxic contaminants and typically require substantial energy inputs.[1] To align with the principles of sustainable chemistry, it is essential to develop more efficient reaction conditions and advanced catalytic systems for pollutant removal, thereby ensuring water quality.[2] Photocatalysis is a light-driven chemical process that occurs when a photocatalyst is activated under light irradiation. This technique has attracted considerable attention due to its simplicity, cost-effectiveness, non-toxicity, high degradation efficiency, and long-term stability. It is widely recognized as a promising strategy for wastewater treatment and environmental protection.[3]

In recent years, semiconductor materials such as TiO_2, ZnO, SnO_2, $g\text{-}C_3N_4$, and perovskites have been extensively investigated for photocatalytic applications in environmental remediation. Among emerging photocatalysts,

**Corresponding author.*
Email: nguyenvankim@qnu.edu.vn, nguyenthivietnga@qnu.edu.vn

https://doi.org/10.52111/qnjs.2026.20106

$Co_x[Fe(CN)_6]_y$ has attracted growing attention and is gradually demonstrating its potential in photocatalysis, showing promise as a candidate for broad environmental applications.

Despite its outstanding advantages–such as strong visible-light absorption, non–toxicity to humans and other organisms, absence of secondary pollution, and ease of recyclability–$Co_x[Fe(CN)_6]_y$ exhibits a major limitation: its high solubility in aqueous media. This characteristic poses significant challenges for its synthesis and practical application.

In 2013, Dwivedi et al.[4] employed gel beads containing cobalt hexacyanoferrate immobilized on micrometer-sized alginate beads (a salt of alginic acid, ($C_6H_8O_6$)) as an adsorbent material for the removal of radioactive contaminants–such as cesium, an element with a half-life spanning several decades–from aqueous solutions. In 2016, K. A. Lin et al.[5] successfully synthesized a series of Prussian blue analogues with the general formula $M(II)_3[M(III)(CN)_6]_2$ (M^{2+} = Co, Cu, Fe, Mn, Ni; M^{3+} = Co, Fe), which exhibited high photocatalytic activity. These materials were capable of efficiently degrading Rhodamine B (RhB) in aqueous solution when activated by peroxymonosulfate (PMS) under neutral conditions. Cobalt-based Prussian blue analogues (PBAs) have shown great potential as efficient catalysts for water-splitting reactions and the degradation of organic pollutants. Moreover, the Co–Fe PBAs retain their original crystalline structure even after multiple recycling cycles, indicating excellent structural stability.

Several studies have employed metal-containing complexes and their isomers as polymeric materials. These isomeric complexes often crystallize in cubic structures and feature metal ions in varying oxidation states.[6] The frameworks of these complexes possess porous structures, which endow them with a high specific surface area, excellent adsorption capacity, and numerous catalytic active sites. As a result, such complexes have been extensively studied across various fields, particularly in photocatalysis.[7] Therefore, the modification of these complexes with semiconductors to develop novel materials exhibiting enhanced photocatalytic activity has attracted significant attention from researchers.

2. EXPERIMENTS

2.1. Chemicals

Chemicals were purchased from Sigma-Aldrich (Germany) with high purity, including cobalt sulfate ($CoSO_4$, ≥ 99.0%), potassium ferrocyanide ($K_4[Fe(CN)_6]$, ≥ 98.5%), melamine ($C_3H_6N_6$, ≥ 99.0%), methylene blue hydrate ($C_{16}H_{18}ClN_3S.xH_2O$, ≥ 97.0%), and ethanol (C_2H_5OH, ≥ 99.9%). All chemicals were used without further purification.

2.2. Materials preparation

2.2.1. Synthesis of g-C_3N_4: Five grams of melamine were ground in an agate mortar and then transferred to a porcelain crucible. The crucible was tightly covered with aluminum foil to minimize sublimation and enhance the condensation efficiency of g-C_3N_4. The sample was heated in a muffle furnace at 550 °C for 2 hours with a heating rate of 10 °C/min. After natural cooling to room temperature, the resulting product–yellowish in color–was collected and labeled as g-C_3N_4.

2.2.2. Synthesis of $Co_2[Fe(CN)_6]$: 5 milliliters of 0.2 M $CoSO_4$ solution were added to a 200 mL glass beaker. Then, 100 mL of 0.05 M $K_4[Fe(CN)_6]$ solution were gradually added at a rate of 5 mL/min under continuous stirring at room temperature. A precipitate formed during the addition. The mixture was stirred for an additional 60 minutes, followed by ultrasonic treatment at 90 °C for 2 hours. The resulting solid was collected by centrifugation and washed repeatedly with distilled water until the pH of the filtrate reached 7. Finally, the sample was dried at 80 °C for 48 hours. The final product was identified as $Co_2[Fe(CN)_6]$.

2.2.3. Synthesis of $Co_2[Fe(CN)_6]$/g-C_3N_4 composite: Cobalt sulfate ($CoSO_4$) was dissolved in deionized water under stirring until fully dissolved. A suitable amount of g-C_3N_4 powder was then added to the solution, followed by stirring and ultrasonication for 60 minutes at room temperature to promote the adsorption of Co^{2+} ions onto the g-C_3N_4 surface. The resulting suspension was centrifuged to collect the solid. Subsequently, a $K_4[Fe(CN)_6]$ solution (with a mass ratio of $K_4[Fe(CN)_6]$ to g-C_3N_4 of 1:3) was added to the solid under continuous stirring at 90 °C for 60 minutes to allow in situ formation of the $Co_2[Fe(CN)_6]$ framework on the g-C_3N_4 matrix. The product was separated by centrifugation, washed thoroughly, and dried at 80 °C for 48 hours to yield a blue solid of $Co_2[Fe(CN)_6]$/g-C_3N_4.

2.3. Characterization

X-ray diffraction (XRD) patterns were recorded using a Bruker D8 Advance diffractometer equipped with a Cu Kα radiation source (λ = 1.540 Å), operating at 30 kV and 0.01 A. Fourier-transform infrared (FTIR) spectra were obtained using a PerkinElmer GX spectrometer. The morphology and elemental composition of the samples were examined by scanning electron microscopy (SEM) and energy-dispersive X-ray spectroscopy (EDS) using a Nova Nano SEM 450 system. UV–Vis diffuse reflectance spectra (UV–Vis DRS) were measured using a Jasco V-770 spectrophotometer, while photoluminescence (PL) spectra were recorded on a Horiba Jobin Yvon FL322 fluorescence spectrometer. The concentration of MB solution was determined by a photometric method using a Jenway 6800 UV–Vis spectrophotometer.

2.4. Photocatalytic activity

The adsorption equilibrium time of MB on the materials was investigated under dark conditions using the following procedure. A total of 0.07 g of the material sample was added to a 250 mL beaker containing 120 mL of MB solution (10 mg/L). The beaker was covered with a wooden enclosure to prevent light exposure and continuously stirred using a magnetic stirrer. At 30-minute intervals, 8 mL of the suspension was withdrawn, centrifuged to separate the supernatant, and the resulting solution was transferred into a vial. The collected samples were labeled as t_0, t_1, t_2, ..., t_8, corresponding to sampling times of 0, 30, 60, ..., and 240 minutes.

The adsorption capacity is calculated using the following equation:

$$q = \frac{(C_i - C_f).V}{m}$$

where q: adsorption capacity at a given time (mg/g); C_i: initial concentration of the solution (mg/L); C_f: concentration of the solution at the given time (mg/L); V: volume of the solution subjected to adsorption (L); m: mass of the adsorbent (g).

A plot of adsorption capacity versus time was drawn to determine the time required to reach adsorption equilibrium. Following the adsorption study, the sample was further exposed to sunlight to evaluate its photocatalytic activity. The degradation efficiency of MB by the materials was calculated using the following equation:

$$H = \frac{C_0 - C_t}{C_0} \times 100\%$$

where C_0 and C_t are the MB concentrations at the initial and selected t- times, respectively.

3. RESULTS AND DISCUSSIONS

3.1. Material characterization

The $Co_2[Fe(CN)_6]$, g-C_3N_4, and $Co_2[Fe(CN)_6]$/g-C_3N_4 samples were characterized by XRD, FTIR, and SEM techniques.

As shown in Figure 1a, the XRD pattern of the $Co_2[Fe(CN)_6]$ sample displays distinct diffraction peaks at 2θ = 25.27°, 35.92°, 44.45°, 51.53°, 54.01°, and 58.38°, which correspond to the (220), (400), (422), (440), (620), and (622) crystal planes, respectively. These results

https://doi.org/10.52111/qnjs.2026.20106

are in good agreement with previous reports on $Co_2[Fe(CN)_6]$. $Co_2[Fe(CN)_6]$ exhibits high crystallinity with characteristic diffraction peaks corresponding to the Prussian blue analogue (PBA) phase, in accordance with JCPDS card No. 77-1161.[8-10] The formation of the PBA-type $Co_2[Fe(CN)_6]$ material from its precursors can be represented by the following reaction equation:

$$2CoSO_4 + K_4[Fe(CN)_6] \rightarrow Co_2[Fe(CN)_6]\downarrow + 2K_2SO_4 \quad (*)$$

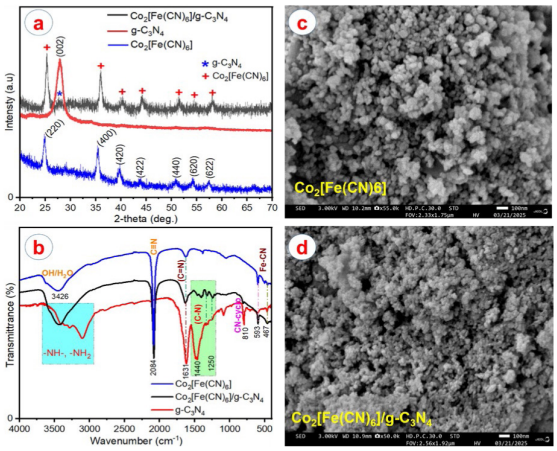

Figure 1. (a) XRD patterns; (b) FTIR spectra; (c, d) SEM images of $Co_2[Fe(CN)_6]$, g-C_3N_4, and the $Co_2[Fe(CN)_6]$/g-C_3N_4 composite.

The XRD pattern of pure g-C_3N_4 exhibits a prominent diffraction peak at $2\theta = 27.4^o$, which corresponds to the (002) crystal plane. This peak is attributed to the interlayer stacking of conjugated aromatic systems in the graphitic carbon nitride structure. The $Co_2[Fe(CN)_6]$/g-C_3N_4 composite clearly exhibits the characteristic diffraction peaks of both constituent materials, $Co_2[Fe(CN)_6]$ and g-C_3N_4. Moreover, no additional crystalline phases are detected, indicating that the composite consists solely of these two components. This result is consistent with previously reported studies on PBA/g-C_3N_4 materials.[8]

The FTIR spectra of the samples are presented in Figure 1b. The g-C_3N_4 sample exhibits a distinct absorption band at 810 cm^{-1}, which is attributed to the out-of-plane bending vibration of C–N bonds within the tri-s-triazine (heptazine) units–the fundamental structural motifs of the graphitic carbon nitride framework.[11,12] The sharp absorption bands in the region of 1250–1631 cm^{-1} are attributed to the stretching vibrations of C–N and C=N bonds within the aromatic rings of the heptazine-based structure.[13,14] In addition, a broad absorption band in the range of 3100–3400 cm^{-1} is observed, which is attributed to the stretching vibrations of –NH– and $–NH_2$ groups originating from the incompletely condensed structure of g-C_3N_4. The FTIR spectrum of $Co_2[Fe(CN)_6]$ displays several characteristic absorption bands. A strong and sharp peak at 2084 cm^{-1} is attributed to the stretching vibration of the C≡N bond in the cyanide ligands, while a prominent band at 593 cm^{-1} corresponds to the bending vibration of the same group. Additionally, the absorption band at 467 cm^{-1} is ascribed to the stretching vibration of the Fe–CN bond,[15,16] confirming the metal–ligand coordination typical of Prussian Blue analogues (PBAs). Furthermore, a broad absorption band centered around 3426 cm^{-1} is associated with the –OH stretching vibration of water molecules adsorbed on the material surface. For the $Co_2[Fe(CN)_6]$/g-C_3N_4 composite, the characteristic peaks corresponding to both g-C_3N_4 and $Co_2[Fe(CN)_6]$ were clearly observed, indicating the successful integration of the two components. In particular, the intense absorption band at 2084 cm^{-1} (assigned to the –C≡N stretching vibration) remained prominent, while the C–N and C=N stretching vibrations of g-C_3N_4 were also retained. These observations confirm that the key structural features of both phases were preserved in the composite. Moreover, the absence of new absorption bands or significant peak shifts suggests that the interaction between $Co_2[Fe(CN)_6]$ and g-C_3N_4 is primarily physical in nature, possibly involving electrostatic attractions or hydrogen bonding. This result is in good agreement with the XRD data.

The SEM images of the $Co_2[Fe(CN)_6]$ sample (Figure 1c) and the $Co_2[Fe(CN)_6]$/g-C_3N_4 composite (Fig. 1d) reveal distinct

morphological characteristics. The pristine $Co_2[Fe(CN)_6]$ exhibits a granular morphology composed of irregularly shaped, densely packed nanoparticles with a pronounced tendency toward agglomeration. The surface of the material appears relatively rough and compact, which may limit the accessibility of active sites for catalytic processes. In contrast, the $Co_2[Fe(CN)_6]$/g-C_3N_4 composite exhibited a more porous architecture with significantly reduced particle agglomeration. The nanoparticles were more uniformly dispersed, with increased interparticle voids, likely attributed to the structural support provided by the g-C_3N_4 matrix. This morphology suggests enhanced textural properties, such as a larger specific surface area and improved accessibility to active sites-factors that are critical for adsorption and photocatalytic performance. The morphological differences between the two samples provide clear evidence for the successful incorporation of $Co_2[Fe(CN)_6]$ into the g-C_3N_4 matrix. This integration effectively suppresses excessive particle agglomeration, enhances interfacial contact, and facilitates charge transfer during the photocatalytic process. These observations are consistent with the XRD and FTIR analyses, further confirming the formation of a structurally and functionally synergistic composite material.

The EDS spectra in Figure 2 and Table 1 confirm the elemental composition of the samples.

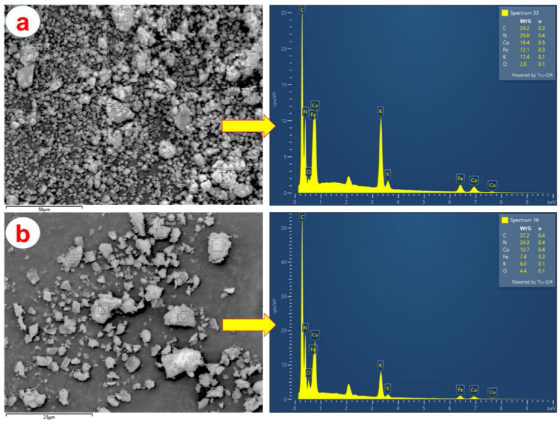

Figure 2. EDS spectra of (a) the $Co_2[Fe(CN)_6]$ sample and (b) the $Co_2[Fe(CN)_6]$/g-C_3N_4 composite.

Both the $Co_2[Fe(CN)_6]$ and $Co_2[Fe(CN)_6]$/g-C_3N_4 samples exhibit characteristic peaks of Co, Fe, C, and N, consistent with the expected structure of Prussian Blue analogues (PBA). Additionally, minor signals of K and O are observed. The presence of K is attributed to residual $K_4[Fe(CN)_6]$ precursor, while the O signal likely originates from surface-adsorbed moisture (H_2O). In the $Co_2[Fe(CN)_6]$/g-C_3N_4 composite, the increased intensities of C and N peaks are ascribed to the contribution of the g-C_3N_4 matrix, while the decreased Co and Fe contents suggest effective dispersion of the PBA phase on the g-C_3N_4 surface. These findings confirm the successful formation of the composite material.

Table 1. Elemental composition of $Fe_3[Fe(CN)_6]_2$ and $Fe_3[Fe(CN)_6]_2$/g-C_3N_4.

$Co_2[Fe(CN)_6]$		$Co_2[Fe(CN)_6]$/g-C_3N_4	
Element	Weight %	Element	Weight %
C	29.2	C	37.2
N	29.0	N	34.3
Co	16.4	Co	10.7
Fe	12.1	Fe	7.4

The EDS-mapping (Figure 3a) results show that Co, Fe, C, and N elements are uniformly distributed across the sample surface, indicating the successful integration and homogeneous dispersion of $Co_2[Fe(CN)_6]$ within the g-C_3N_4 matrix. No significant aggregation or phase separation was observed, suggesting strong interfacial compatibility between the two components. This uniform distribution supports the structural integrity of the composite and correlates well with the results obtained from XRD, FTIR, and SEM, reinforcing the successful synthesis of a well-dispersed hybrid photocatalyst.

https://doi.org/10.52111/qnjs.2026.20106

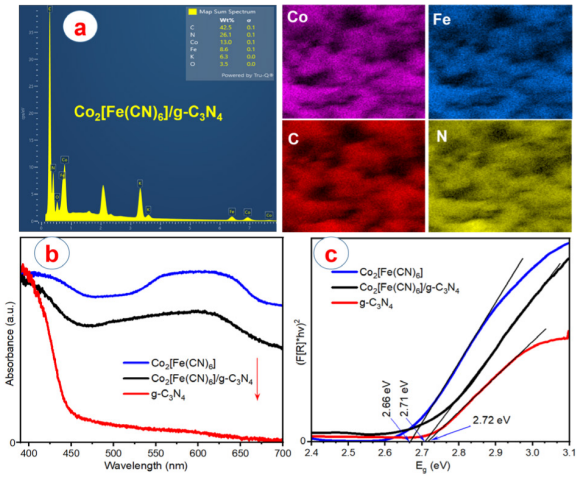

Figure 3. (a) Elemental mapping images of Co, Fe, C, and N for the $Co_2[Fe(CN)_6]/g\text{-}C_3N_4$ composite, (b) UV–Vis DRS spectra and (c) band gap energy of the materials.

The UV–Vis DRS (Figures 3b,c) reveal that all the materials exhibit absorption edges within the visible light region. Notably, the $Co_2[Fe(CN)_6]$ and $Co_2[Fe(CN)_6]/g\text{-}C_3N_4$ samples show extended absorption edges reaching up to approximately 700 nm, which is consistent with the characteristic charge transfer transitions between Fe(II) and Fe(III):[17]

$$[Fe(CN)_6]^{4-} \rightleftharpoons [Fe(CN)_6]^{3-} + e^-$$

The band gap energy (E_g) of the materials was also estimated using this method. Accordingly, the band gap values of $Co_2[Fe(CN)_6]$, $g\text{-}C_3N_4$, and the $Co_2[Fe(CN)_6]/g\text{-}C_3N_4$ composite were determined to be 2.66 eV, 2.72 eV, and 2.71 eV, respectively.

3.2. Photocatalytic activity

The photocatalytic performance of the materials was evaluated through the degradation of MB under sunlight irradiation, with the results illustrated in Figure 4a. After 210 minutes of exposure, the $Co_2[Fe(CN)_6]/g\text{-}C_3N_4$ composite exhibited a degradation efficiency of 93.38%, outperforming both pristine $g\text{-}C_3N_4$ and $Co_2[Fe(CN)_6]$ (Figure 4b). In addition, to compare the MB degradation rates among the materials, the photodegradation kinetics were analyzed (Figure 4c and Table 2). Under identical illumination conditions, the degradation rate of MB using the $Co_2[Fe(CN)_6]/g\text{-}C_3N_4$ composite was approximately five times higher than that of $Co_2[Fe(CN)_6]$ and more than 19 times higher than that of pristine $g\text{-}C_3N_4$. This significant enhancement is attributed to the effective suppression of the rapid recombination of photogenerated electron–hole pairs, a common limitation in single-component $g\text{-}C_3N_4$ photocatalysts, as confirmed by the photoluminescence (PL) spectrum shown in Figure 4d.

Table 2. Results of MB degradation by the materials.

Materials	Photodegradation (%)	Rate constant, k (min^{-1})	Regression coefficient (R^2)
$g\text{-}C_3N_4$	13.91	$0.06.10^{-2}$	0.95
$Co_2[Fe(CN)_6]$	38.74	$0.24.10^{-2}$	0.99
$Co_2[Fe(CN)_6]/g\text{-}C_3N_4$	93.38	$1.16.10^{-2}$	0.98

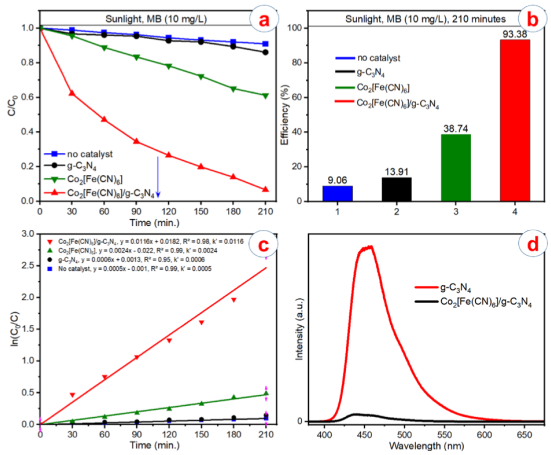

Figure 4. (a-c) Photocatalytic degradation of MB over $Co_2[Fe(CN)_6]$, $g\text{-}C_3N_4$, and $Co_2[Fe(CN)_6]/g\text{-}C_3N_4$; (d) PL spectra of the corresponding materials.

The photoluminescence (PL) spectra of $g\text{-}C_3N_4$ and the $Co_2[Fe(CN)_6]/g\text{-}C_3N_4$ composite were recorded under 365 nm excitation to evaluate the separation and recombination behavior of photoinduced electron–hole pairs (e^-/h^+). In the spectrum, pristine $g\text{-}C_3N_4$ exhibits a strong emission peak around 400–550 nm,

which is indicative of the rapid recombination of photogenerated charge carriers. Notably, the PL intensity of the $Co_2[Fe(CN)_6]$/g-C_3N_4 composite is significantly quenched compared to pure g-C_3N_4. This pronounced reduction in emission intensity suggests that the incorporation of $Co_2[Fe(CN)_6]$ effectively suppresses the recombination of charge carriers. As an efficient electron acceptor, $Co_2[Fe(CN)_6]$ facilitates charge transfer and enhances charge separation at the heterojunction interface with g-C_3N_4. In summary, the PL analysis confirms that the formation of the $Co_2[Fe(CN)_6]$/g-C_3N_4 composite improves electron–hole separation and reduces charge recombination, thereby enhancing the photocatalytic performance by making more charge carriers available for surface reactions. This property broadens the potential applications of the $Co_2[Fe(CN)_6]$/g-C_3N_4 composite in the field of photocatalysis.

3.3. Photocatalytic reaction mechanism

To investigate the photocatalytic reaction mechanism, various scavengers were employed to identify the main reactive species involved. Tert-butyl alcohol (TBA) was used as a scavenger for hydroxyl radicals (·OH), 1,4-benzoquinone (BQ) for superoxide radical anions ($\cdot O_2^-$), ammonium oxalate (AO) for photogenerated holes (h^+), and dimethyl sulfoxide (DMSO) for photogenerated electrons (e^-).[18] A quenching agent solution with an initial concentration of 10 mmol/L and a volume of 2 mL was added at the onset of light irradiation. As shown in Figure 5a, the presence of TBA and AO led to a noticeable decrease in the photocatalytic degradation of MB by the $Co_2[Fe(CN)_6]$/g-C_3N_4 composite, compared to the control sample without any scavenger. This can be attributed to the quenching effects of ammonium oxalate (AO) on photogenerated holes (h^+) and of 1,4-benzoquinone (BQ) on superoxide radical anions ($\cdot O_2^-$), which significantly suppressed the activity of these reactive species in solution and thus reduced photocatalytic efficiency. These findings suggest that h^+ and $\cdot O_2^-$ are the primary active species responsible for the MB degradation process. Thus, the integration of $Co_2[Fe(CN)_6]$ and g-C_3N_4 into a composite structure resulted in $Co_2[Fe(CN)_6]$/g-C_3N_4, which possesses critical properties for facilitating the generation of h^+ and $\cdot O_2^-$ radicals, while simultaneously suppressing the recombination of photogenerated electron–hole pairs during the photocatalytic degradation of MB.

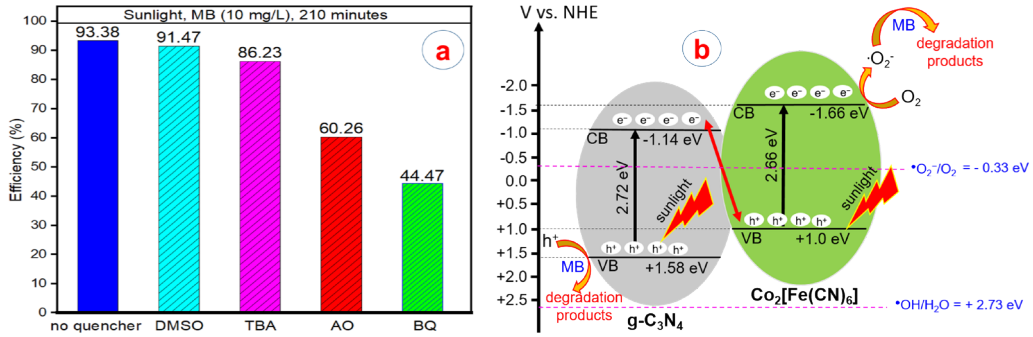

Figure 5. (a) Photocatalytic degradation of MB on $Co_2[Fe(CN)_6]$/g-C_3N_4 in the presence of various scavengers, and (b) Proposed Z-scheme mechanism for the photocatalytic activity of the $Co_2[Fe(CN)_6]$/g-C_3N_4 composite.

The valence band (VB) and conduction band (CB) positions of g-C_3N_4 and $Co_2[Fe(CN)_6]$ can be estimated using the following equations:

$$E_{VB} = \chi - E^e + 0.5E_g$$

$$E_{CB} = E_{VB} - Eg$$

where χ is the absolute electronegativity of the semiconductor (defined as the arithmetic mean of the electron affinity and the first ionization energy of the constituent atoms), E^e is the energy of free electrons on the hydrogen scale (4.5 eV), and E_g is the band gap energy of the semiconductor.

According to Wu et al.,[19] the absolute electronegativity (χ) of g-C_3N_4 is 4.72 eV. Based on Mulliken's theory, the electronegativity χ of a semiconductor can be accurately calculated using the following formula:

$$\chi = E_{vacuum} - \frac{E_g}{2}$$

Applied to $Co_2[Fe(CN)_6]$:

+ $E_g \approx 2.66$ eV (as determined from the UV–Vis DRS spectra);

+ $E_{vacuum} \approx 5.5$ eV.[20]

The calculated absolute electronegativity (χ) is 4.17 eV.

Based on the calculations, the conduction band (CB) and valence band (VB) edge potentials of g-C_3N_4 are estimated to be −1.14 eV and +1.58 eV, respectively. Similarly, the CB and VB edge potentials of $Co_2[Fe(CN)_6]$ are calculated to be −1.66 eV and +1.00 eV, respectively.

On this basis, the separation of photogenerated electron–hole pairs and the formation of reactive radicals in the $Co_2[Fe(CN)_6]$/g-C_3N_4 composite under illumination are illustrated in Figure 5b (Z-scheme). Under light irradiation, both semiconductor materials are photoexcited and generate electron–hole pairs. The photogenerated electrons in the conduction band (CB) of g-C_3N_4 tend to recombine with the holes in the valence band (VB) of $Co_2[Fe(CN)_6]$. This recombination occurs at the contact interface, leading to the accumulation of electrons in the conduction band (CB) of $Co_2[Fe(CN)_6]$ and holes in the valence band (VB) of g-C_3N_4. Consequently, the photogenerated charge carriers are spatially separated across the two semiconductors, while maintaining strong redox potentials. The electrons in the conduction band (CB) of $Co_2[Fe(CN)_6]$ reduce O_2 to superoxide radicals ($\cdot O_2^-$), which subsequently contribute to the degradation of MB. In contrast, the holes in the valence band (VB) of g-C_3N_4, due to their insufficient oxidation potential, are unable to oxidize H_2O to generate hydroxyl radicals (·OH), but can directly oxidize MB molecules. Accordingly, the photocatalytic degradation of MB may involve the following processes:

$$Co_2[Fe(CN)_6]/g\text{-}C_3N_4 + h\nu \rightarrow e^- + h^+$$

$$[Fe(CN)_6]^{4-} \rightleftharpoons [Fe(CN)_6]^{3-} + e^-$$

$$e^- + O_2 \rightarrow \cdot O_2^-$$

$$\cdot O_2^- + MB \rightarrow \text{decomposition products}$$

$$h^+ + MB \rightarrow \text{decomposition products}$$

This mechanism satisfactorily explains the reduced recombination of photogenerated electron–hole pairs on the g-C_3N_4 component of the $Co_2[Fe(CN)_6]$/g-C_3N_4 composite, as confirmed by the photoluminescence (PL) analysis (Figure 4d) and the photocatalytic performance results (Figure 5a). This suppression of charge carrier recombination subsequently enhances the photocatalytic degradation efficiency of MB by the composite under light irradiation.

4. CONCLUSIONS

Nano-sized $Co_2[Fe(CN)_6]$ and the $Co_2[Fe(CN)_6]$/g-C_3N_4 composite were successfully synthesized. The corresponding band gap energies were determined to be 2.66 eV for $Co_2[Fe(CN)_6]$, 2.72 eV for g-C_3N_4, and 2.71 eV for the composite. Under natural sunlight irradiation for 210 minutes, the $Co_2[Fe(CN)_6]$/g-C_3N_4 composite exhibited a photocatalytic degradation efficiency of 93.38% for methylene blue in aqueous solution, significantly outperforming the individual components $Co_2[Fe(CN)_6]$ and g-C_3N_4. The enhanced photocatalytic activity of the composite is mainly attributed to the effective suppression of photogenerated electron–hole recombination. A Z-scheme mechanism for the photocatalytic degradation of methylene blue over the $Co_2[Fe(CN)_6]$/g-C_3N_4 composite was proposed and discussed in detail by the authors.

Acknowledgments

This research is conducted within the framework of science and technology projects at institutional level of Quy Nhon University under the project code T2025.887.07.

REFERENCES

1. Ö. Arar, Ü. Yüksel, N. Kabay, M. Yüksel. Various applications of electrodeionization (EDI) method for water treatment - a short review, *Desalination*, **2014**, *342*, 16-22.
2. É. N. Santos, Z. László, C. Hodúr, G. Arthanareeswaran. Photocatalytic membrane filtration and its advantages over conventional approaches in the treatment of oily wastewater: a review, *Asia-Pacific Journal of Chemical Engineering*, **2020**, *2533*, 11-19.
3. L. Jiang, Y. Wang, C. Feng. Application of photocatalytic technology in environmental safety, *Procedia Engineering*, **2012**, *45*, 993–997.
4. D. Charu, K. P. Sanjay, K. Manmohan, C. T. Subhash, N. B. Parma. Potassium cobalthexacyanoferrate–gel beads for cesium removal: kinetics and sorption studies, *RSC Advances*, **2013**, *3*, 22102-22110.
5. K. A. Lin, B. Chen, C. Chen. Evaluating prussian blue analogues M II 3[MIII(CN)6]2 (MII = Co, Cu, Fe, Mn, Ni; MIII = Co, Fe) as activators for peroxymonosulfate in water, *RSC Advances*, **2016**, *95*, 1–36.
6. F. Karadas, H. E. Faki, E. Deniz, C. T. Yavuz, S. Aparicio, M. Atilhan. CO_2 adsorption studies on Prussian blue analogues, *Microporous and Mesoporous Materials*, **2012**, *162*, 91-97.
7. X. Li, J. Liu, A. I. Rykov, H. Han, C. Jin, X. Liu, J. Wang. Excellent photo-Fenton catalysts of Fe-Co prussian blue analogues and their reaction mechanism study, *Applied Catalysis B: Environmental*, **2015**, *179*, 196-205.
8. H. T. L. Lan, A. N. Son, D. N. Trung, C. T. L. Van, V. C. Hai, B. N. Ngoc, P. T. L. Thao. Prussian blue analogues of A_2[Fe(CN)6] (A: Cu^{2+}, Co^{2+}, and Ni^{2+}) and their composition-dependent sorption performances towards Cs^+, Sr^{2+}, and Co^{2+}, *Journal of Nanomaterials*, **2021**, *20213*, 1-12.
9. S. Adak, L. L. Daemen, M. Hartl, D. Williams, J. Summerhill, H. Nakotte. Thermal expansion in 3d-metal prussian blue analogs - a survey study, *Journal of Solid State Chemistry*, **2011**, *184*, 2854-2861.
10. S. Xu, X. Qian, G. Li. Size and morphology-controlled $Ni_2[Fe(CN)_6]\cdot xH_2O$ prussian blue analogue fabricated via a hydrothermal route, *Materials Research Bulletin*, **2008**, *43*, 135-140.
11. E. Jang, D. W. Kim, S. H. Hong, Y. M. Parkc, T. J. Park. Visible light-driven g-C_3N_4@ZnO heterojunction photocatalyst synthesized via atomic layer deposition with a specially designed rotary reactor, *Applied Surface Science*, **2019**, *487*, 206-210.
12. M. Kim, S. Hwang, J. S. Yu. Novel ordered nanoporous graphitic carbon nitride with g-C_3N_4 stoichiometry as a support for Pt-Ru anode catalyst in DMFC, *Journal of Materials Chemistry*, **2007**, *17*, 1656–1659.
13. N. V. Kim, N. T. V. Nga, T. T. T. Phuong, N. L. Tuan, V. Vien. Synthesis of g-C_3N_4/ZnO composites with enhanced photocatalytic activity under visible light, *Vietnam Journal of Chemistry*, **2018**, *56*, 220-225.
14. F. Dong, Y. Li, Z. Wang, W. K. Ho. Enhanced visible light photocatalytic activity and oxidation ability of porous graphene-like g-C_3N_4 nanosheets via thermal exfoliation, *Applied Surface Science*, **2015**, *358*, 393-403.
15. X. Li, J. Liu, A. I. Rykov, H. Han, C. Jin, X. Liu, J. Wang. Excellent photo-Fenton catalysts of Fe–Co Prussian blue analogues and their reaction mechanism study, *Applied Catalysis B: Environmental*, **2015**, *179*, 196-205.
16. Y. Chen, R. C. Zhou, Y. H. Wan, J. W. Hao, H. R. You, X. M. Liu, H. Yang. $KCo_xMn_{1-x}[Fe(CN)_6]$/Carbon nanotube composite as high capacity anode for Li-ion batteries, *Journal of Electroanalytical Chemistry*, **2021**, *887*, 115151.

17. S. Jiao, J. Tuo, H. Xie, Z. Cai, S. Wang, J. Zhu. The electrochemical performance of $Cu_3[Fe(CN)_6]_2$ as a cathode material for sodium-ion batteries, *Materials Research Bulletin*, **2017**, *86*, 194-200.

18. L. Shi, L. Liang, J. Ma, F. Wang, J. Sun. Remarkably enhanced photocatalytic activity of ordered mesoporous carbon/g-C_3N_4 composite photocatalysts under visible light, *Dalton Transactions*, **2014**, *43*, 7236-7244.

19. Y. Wu, L. Tao, J. Zhao, X. Yue, Y. Li, C. Wang. TiO_2/g-C_3N_4 nanosheets hybrid photocatalyst with enhanced photocatalytic activity under visible light irradiation, *Research on Chemical Intermediates*, **2016**, *42*, 3609-3624.

20. L. C. Wang, P. Y. Chiou, Y. P. Hsu, C. L. Lee, C. H. Hung, Y. H. Wu, W. J. Wang, G. L. Hsieh, Y. C. Chen, L. C. Chang, et al. Prussian blue analog with separated active sites to catalyze water driven enhanced catalytic treatments, *Nature Communications*, **2023**, *14*, 4709.

© 2026 by the authors. This Open Access Article is licensed under the Creative Commons Attribution-NonCommercial 4.0 International (CC BY-NC 4.0) license (https://creativecommons.org/licenses/by-nc/4.0/).